

High-precision interferometric measurement of rapid temperature changes in convective flow

Xinyang Ge^{1*}, Joanna A. Zielińska^{1,2} and Sergio Maldonado^{1*}

¹Faculty of Engineering and Physical Sciences, University of Southampton, Southampton, SO16 7QF, UK.

²Photonics Laboratory, ETH Zurich, Zurich, CH-8093, Switzerland.

*Corresponding author(s). E-mail(s): xg2n17@soton.ac.uk; s.maldonado@soton.ac.uk;
Contributing authors: jzielinska@ethz.ch;

Abstract

Using interferometry, we measure rapid temperature variations in convective flow to within a few mK. This is enabled by the fast response time and high sensitivity of the interferometer to minute changes in the refractive index of the test fluid caused by temperature variations. These features allow us to detect the signature of fine fluid dynamical patterns in convective flow in a fully non-intrusive manner. For example, we are able to observe an asymmetry in the rising thermal plume (i.e. an asynchronous arrival of two counter-rotating vortices at the measurement location), which is not possible to resolve with more traditional (and invasive) techniques, such as RTD (Resistance Temperature Detector) sensors. These findings, and the overall reliability of our method, are further corroborated by means of Particle Image Velocimetry and Large Eddy Simulations. The non-intrusive nature of this method, along with its robustness and the ability to readily yield real-time, highly accurate measurements, render this technique very attractive for a wide range of applications in experimental fluid dynamics.

Keywords: Interferometry, Convective flow, Optical metrology, Temperature measurement

1 Introduction

Reliable measurement of temperature in fluids is important for a wide range of applications, from industrial (e.g. power plants, heat exchangers, chemical industries) to basic scientific research (Ross et al, 2001; Abram et al, 2018; Laffont et al, 2018). Fluid temperature is conventionally measured via intrusive instrumentation. Thermocouples, thermistors and resistance temperature detectors (RTDs) are popular examples of instruments which measure fluid temperature by immersion of a physical probe. While this may not be problematic for many industrial applications,

when studying fluid dynamics from a scientific perspective, this intrusiveness may be undesirable since the probes may disturb local flow patterns. Also, these sensors typically have moderate to poor accuracy. While RTDs are generally considered accurate for most applications, their slow response time prevents them from capturing fast changes in fluid temperature (Goumopoulos, 2018), of the type expected in turbulent flows. Another class of temperature sensors are based on optical fibers (Fernandez-Valdivielso et al, 2003; Rizzolo et al, 2017; Kim et al, 2018; Childs et al, 2000), which offer advantages such as small dimensions, capability of multiplexing, chemical

inertness, and immunity to electromagnetic fields (Roriz et al, 2020). It must be noted, however, that while optical fibre based sensors can be as small as a fraction of a millimetre in diameter (Drusová et al, 2021), they must be immersed in the test fluid, making them invasive instruments. Another intrusive technique is acoustic thermometry, which relies on the measurement of the speed of sound in a given fluid (Wang et al, 2018; Moldover et al, 2014). The response time of this technique is determined by the time traveled by a probe sound wave, in turn given by the thickness of the sample volume. This method can attain a precision of up to ± 0.015 K with a sampling frequency of 5 Hz (Wang et al, 2018).

When it is not possible or desirable for sensors to be in direct contact with the test fluid, a non-intrusive method may be used, such as laser-induced fluorescence (LIF) or interferometry. LIF (originally proposed by Tango et al 1968) works by using laser light to excite a fluorescent dye, which subsequently fluoresces at a different wavelength, revealing temperature changes (Banks et al, 2019). LIF can be used to obtain two- or three-dimensional images (Taylor and Lai, 2021), with accuracy in thermofluid applications of up to 0.17 K (Sakakibara and Adrian, 2004).

Interferometric techniques for visualisation and analysis of transparent fluid flows are non-invasive, fast and extremely sensitive. These include holographic interferometry (HI) and standard interferometry (SI). Interferometric methods extract fluid properties (e.g. temperature) from spatial and/or temporal interference between two laser beams, one of which passes through the test fluid (the other one being the reference). In HI, the interference pattern between two laser beams is recorded on a camera and used to reconstruct the optical phase distribution in the observed area, which directly maps onto 2D temperature distribution within the field of view of the instrument. Several authors have employed HI to understand convection-based heat transfer phenomena around horizontally placed heating rods (Ashjaee et al, 2007; Ashjaee and Yousefi, 2007; Herraes and Belda, 2002; Narayan et al, 2017) as well as temperature profiles during liquid cooling and heating processes (Wang et al, 2022; Wu et al, 2013; Guerrero-Mendez et al, 2016). These investigations have successfully extracted temperature variations in the fluid, with reported

accuracies ranging from 0.20 K (Guerrero-Mendez et al, 2016) to 0.42 K (Wu et al, 2013). Most studies have been limited to laminar flows, and the reported experimental data are recorded under steady-state conditions after the initial transients have died out. This may be due to the fact that, in dynamic measurements, HI performance is limited, as large phase gradients across the beam (which may occur in turbulent flow settings) may lead to non-distinguishable interference structure and errors in the interpretation of fringe patterns (Wilkie and Fisher, 1963; Lira and Vest, 1987).

Unlike HI, SI does not provide spatial information about the distribution of fluid properties such as temperature. Instead, in SI the temporal interference between probe and reference beams is observed using a single-pixel detector, which provides necessary information to measure temporal variations of the optical path length in one location. Continuous modulation of the reference arm length enables monitoring of the interference visibility, which provides information about the performance of the instrument (which may be affected by phase gradients perpendicular to the probe beam's direction of propagation). This is advantageous for highly non-uniform flow settings, permitting measurements in the presence of large phase gradients (albeit with reduced sensitivity). What is more, SI is relatively simple and economic, with data processing requirements being significantly less computationally demanding than those of HI. These characteristics are desirable for real-time measurements of rapid temperature variations in fluids.

In this paper, we apply SI as a non-intrusive, fast-response method to study convective flow in water induced by a horizontal heating rod. We are able to characterise the transient heat transfer phenomenon, including the raising thermal plume (and consequent large temperature gradients), and observe the signature of fluid dynamical patterns which are too fast to be recorded by other methods such as RTD sensors. The structure of the paper is as follows. In Section 2, we explain the experimental setup and the procedure to extract temperature changes from shifts in interference patterns. Then, Section 3 presents the results of a slowly varying temperature experiment in static fluid, which establishes the method's reliability and sensitivity. Next, in Section 4, we apply our

technique to convective flow, and compare the obtained results against those from RTD sensors, further enhancing our analysis by use of Particle Image Velocimetry and Large Eddy Simulations. Concluding remarks are presented in Section 5.

2 Methodology

2.1 Interferometry: basic theory

In most interferometers, light from a single coherent source is split into two beams that travel via different optical paths, which are then recombined to produce an interference pattern. The resulting interference fringes provide information about the difference in optical path lengths with a precision of a fraction of the wavelength of light.

Here, we measure water temperature using a Michelson interferometer. The probe arm of the interferometer passes through the water tank, while the second (reference) arm path bypasses the tank. The interferometer measures the phase difference between the two arms, which depends on the refractive index of water, in turn given by its temperature.

The experimental setup is shown in Fig. 1(a). A laser beam is split into two equal-power components with the help of a beam-splitter. One of the beams passes through the water tank and is reflected off a stationary mirror, while the other one is reflected off a mirror mounted on a piezoelectric actuator, fed by a voltage signal shown in Fig. 1(b). The interference signal $S(t)$ is detected by a photodetector. The signal $S(t)$ consists of fringes, resulting from linear phase ramps (i.e. linear piezo displacement in time; see $V(t)$ curve in Fig. 1b) introduced by the piezoelectric transducer (PZT). Each time the PZT reverses direction, we observe a ‘turning point’ in the fringe pattern (see times 100, 200 and 300 in Fig. 1(b)).

Interferometry does not provide absolute temperature measurements, but rather variations with respect to time. We detect time variations of the temperature (refractive index) of water by comparing the fringe patterns recorded in different moments in time (consecutive PZT sweeps). A shift of the fringe pattern with respect to the PZT drive signal allows us to deduce the phase difference between the arms, $\phi(t)$, which is expressed

as:

$$\phi(t) = k_0 z_{\text{pzt}}(t) - 2k_0 \int_0^l n_w(t) dz + \phi_0(t), \quad (1)$$

where k_0 is the wave-vector in vacuum, $k_0 z_{\text{pzt}}(t)$ is the phase shift introduced by the displacement of the PZT (proportional to $V(t)$), the z coordinate is aligned with the direction of beam propagation through the water tank along a path of length l , and $n_w(t)$ is the refractive index of water (which may vary in time). The term ϕ_0 contains mechanical drifts which affect the lengths of the interferometer arms, as well as phase difference introduced by variations in air temperature.

For small temperature variations $\delta T = T_1 - T_0$, we can approximate the dependence of water refractive index on temperature T_1 as

$$n_w(T_1) \approx n_w(T_0) + \left. \left(\frac{\partial n}{\partial T} \right) \right|_{T_0} \delta T, \quad (2)$$

where $\partial n_w / \partial T = -9.6 \times 10^{-5} \text{ K}^{-1}$ within the range of 285 to 305 K at 101,325 Pa (Fernández-Prini and Dooley, 1997). Note that $\partial n / \partial T$ for air is approximately $-9 \times 10^{-7} \text{ K}^{-1}$ (Ciddor, 1996) (dry air, 450 ppm CO₂), such that the experiments described in this paper are much more sensitive to water than to air temperature changes (by two orders of magnitude) that may occur in the lab.

Note that the temperature variation deduced from $\phi(t)$ corresponds to the average change along the beam path (inside the water).

The signal $S(t)$ detected by the photodiode (see PD in Fig. 1) and $\phi(t)$ are related via:

$$S(t) = \eta \left[I_1 + I_2 + 2\sqrt{I_1 I_2} \gamma \cos(\phi(t)) \right], \quad (3)$$

where I_1 and I_2 are the optical intensities corresponding to the probe and reference beams, respectively, and γ is the absolute value of the first order normalized correlation function between probe and reference fields (Mandel and Wolf, 1995). The calibration factor η converts the signal to Volts. The two beams have approximately equal power, such that:

$$I_1 \approx I_2 = \frac{S_0}{2\eta}, \quad (4)$$

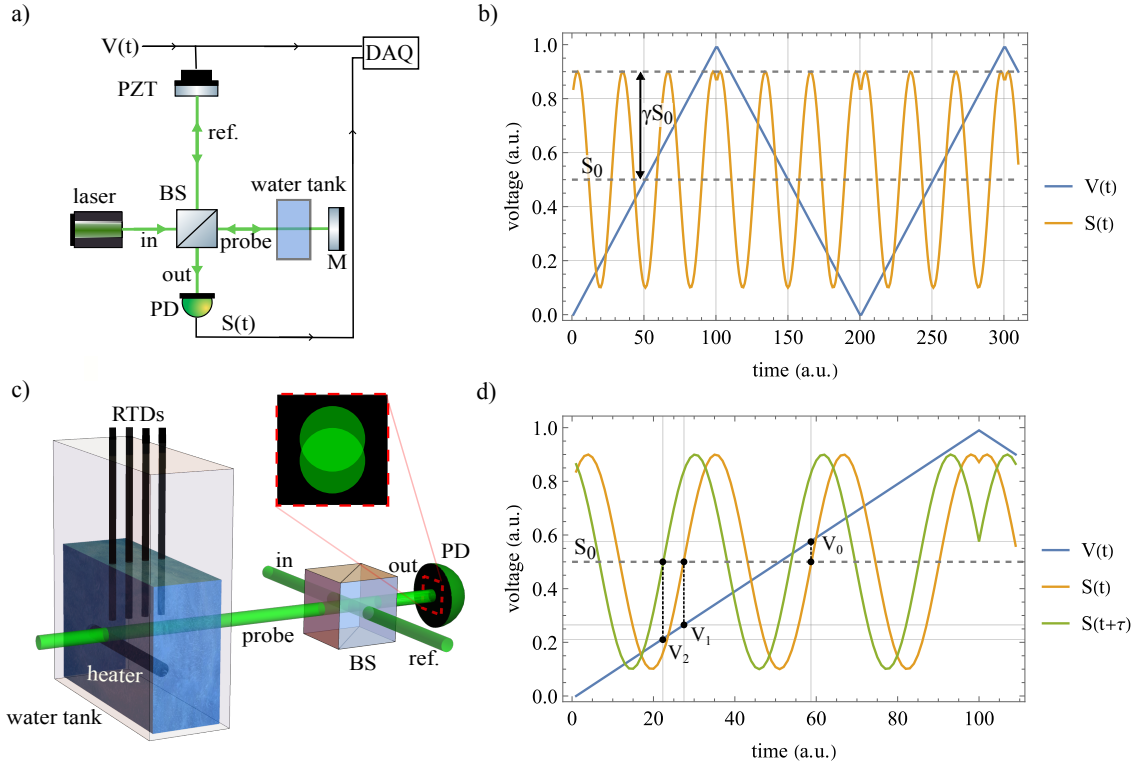


Fig. 1 **a)** Experimental setup of the interferometer. The reference arm length is controlled using a piezoelectric actuator driven by a voltage signal $V(t)$. The probe arm passes twice through the water tank. Abbreviations: PZT - piezoelectric actuator, M - mirror, BS - non-polarising 50:50 beamsplitter, PD - photodetector, DAQ - data acquisition device. **b)** Oscilloscope view of the PZT driving voltage, $V(t)$, and signal recorded on the detector PD, $S(t)$. **c)** 3D render of the setup, showing approximate position of the heating rod and RTD sensors inside the water tank, as well as a close-up schematic view of the overlap between probe and reference beams at the PD. **d)** Illustration of the method for extracting temperature changes from interference pattern shifts; $S(t)$ and $S(t + \tau)$ are PD-detected signals during subsequent piezo strokes.

where S_0 is the DC part of the signal $S(t)$ (see Fig. 1b). The amplitude of the interference fringes relative to S_0 (interference visibility) is dictated by γ . Unit visibility ($\gamma = 1$) occurs when the spatial coherence (overlap between probe and reference beams) is perfect and the path length difference between probe and reference beams is much smaller than the coherence length. In this work the latter is always true, i.e. our anticipated optical path length differences are always well within the coherence length, which for our laser source is equal to the path length difference resulting from a water temperature change of 59 K. The interference visibility in our experiment is therefore limited by spatial misalignment between the two beams and wavefront distortion introduced by water, which results in imperfect overlap of probe

and reference beams at the detector (see inset in Fig. 1c).

The method for extracting temperature changes from the fringe pattern is depicted in Fig. 1d. We calibrate the PZT using the fact that a change of (double-pass) path length difference of one wavelength is equivalent to the shift of the sinusoidal signal pattern by one period. Therefore, a voltage change of $|V_1 - V_0|$ (see Fig. 1d) corresponds to a single-pass path length difference of $\lambda/2$, yielding a calibration factor $\alpha = \frac{\lambda}{2|V_1 - V_0|}$. The temporal change in the refractive index (integrated over l) corresponding to a voltage change $V_2 - V_1$ can then be obtained from:

$$\int_0^l (n_w(t + \tau) - n_w(t)) dz = \alpha(V_2 - V_1), \quad (5)$$

where V_1 is the ‘ S_0 -crossing’ of the signal at time t and V_2 corresponds to the subsequent piezo stroke at time $t+\tau$ (see Fig. 1d). Finally, we can calculate the temperature change as:

$$\delta T = T(t + \tau) - T(t) = \frac{\alpha}{l} (V_2 - V_1) \left(\frac{\partial n_w}{\partial T} \right)^{-1}, \quad (6)$$

where $T(t)$ denotes average water temperature along the beam. In our experiments, we sample temperature changes sufficiently fast so that $|V_2 - V_1| < |V_1 - V_0|$ is always satisfied.

3 Static fluid experiment

As a first assessment of the proposed technique, we compare its performance against that of state-of-the-art RTD (Resistance Temperature Detector) sensors for a long experiment where water temperature varies slowly. In order to quantify the stability and sensitivity of our technique, we also analyse its Allan variance.

3.1 Experimental setup

A schematic of the experimental setup is illustrated in Fig. 1. The outer dimensions of the glass tank are $0.20 \times 0.10 \times 0.30$ m in length, width and height, respectively. We use a collimated laser with a wavelength of 532 nm and orient the tank such that the laser travels along its length. The beam splitter is a non-polarising cube beam splitter with a 50:50 (Reflectance : Transmission) beam splitting ratio and the moveable mirror is powered by a discrete piezo ring stack with a maximum displacement of $9 \mu\text{m}$ when driven with no load. The piezo actuator is powered by a waveform generator, which can produce different types of waveforms (e.g. triangular, sinusoidal) with varying frequencies. Four Class 1/10 DIN RTD sensors are evenly spaced inside the water with their probes located near the laser path for comparison against the results obtained from the interferometer. The RTDs are connected to a data logger for recording temperature with a 4-wire configuration. Their accuracy is $\pm(0.03 + 0.0005T)^\circ\text{C}$, where T is the surrounding fluid temperature.

The tank is filled with 20 cm of water and the laser beam is placed 5 cm from the bottom of the tank. For this experiment, the piezo is driven with a triangular signal at 40 Hz. The experiment runs

for 13 hrs in order to compare the results from the proposed technique against measurements from RTD sensors in a simple setting where water temperature varies slowly due to ambient temperature changes. The experiments have been performed remotely at night hours to minimise mechanical vibrations induced by human movement. A layer of insulation is also placed underneath the optical table to further reduce possible noise.

3.2 Results

The temperature variations measured by the RTD sensors and inferred from interferometry are compared in Fig. 2. The observed drop in water temperature is entirely due to the drop in room temperature over night (no additional cooling system is employed). The sampling frequency of the data logger for the RTD sensors is 1 Hz, and the reported value is the average of the four sensors. For the interferometry results, we captured a triggered result based on the voltage from the waveform generator every 6 seconds. The data transmission rate of the oscilloscope itself limits this interval. While a different data logger could have been employed for continuous data recording (see Section 4.1), the volume of data corresponding to this 13 hrs long experiment would have been unnecessarily large for post-processing purposes. Recalling that the proposed technique yields temperature changes rather than absolute values, we have fixed the reference temperature at $t = 0$ as equal to that from the RTD sensors. This is the only calibration we carry out. Fig. 2 shows that the two curves agree extremely well; the difference between the methods has an average of only 2.47×10^{-4} K. Most noticeable differences occur right before the auto-recalibration process of the data logger (see inset in Fig. 2). During operation, the RTD data logger measures the amplifier’s internal ‘offset voltage’. If it is found to have drifted by a specified amount ($1\mu\text{V}$), a calibration cycle is performed (dataTaker, 2013). Regardless of the error caused by the data logger drift, the difference between the two methods is within the expected accuracy of the RTD sensors (~ 0.038 K). This comparison against state-of-the-art temperature sensors in a simple setting serves as a confirmation of the high accuracy achieved by the proposed method.

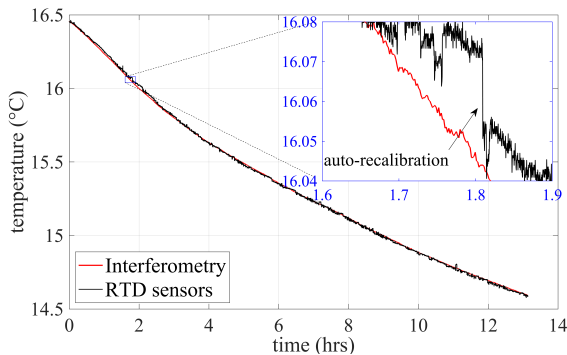


Fig. 2 Comparison of measurements from RTD sensors and interferometry for slowly varying water temperature in static fluid. Differences are barely noticeable (see inset).

3.3 Interferometer stability

We quantify the stability of the interferometer under hydrostatic conditions, which determines the sensitivity of our measurements for a given integration time. A standard method to characterise a sensor’s stability is the two-sample variance, also known as Allan variance (Allan, 1966), which quantifies noise in the system and resulting measurement limitations. For the derivation of the two-sample variance $\sigma_T^2(\tau)$ of a time trace $T(t)$ with length \mathcal{T} , the time trace is split into N equal blocks of length $\tau = \mathcal{T}/N$. For each of these blocks an average value is denoted as $\bar{T}_k^{(\tau)}$, where $k \in (1, \dots, N)$. The Allan variance is the expectation value of the two consecutive values of the block average $\bar{T}_k^{(\tau)}$ as a function of integration time τ :

$$\begin{aligned} \sigma_T^2(\tau) &= \left\langle \frac{1}{2} \left(\bar{T}_{k+1}^{(\tau)} - \bar{T}_k^{(\tau)} \right)^2 \right\rangle \\ &\approx \frac{1}{2(N-1)} \sum_{k=1}^{N-1} \left(\bar{T}_{k+1}^{(\tau)} - \bar{T}_k^{(\tau)} \right)^2. \end{aligned} \quad (7)$$

The result of the Allan variance analysis is shown in Fig. 3, which has been calculated by acquiring data for 2 hrs with a 40 Hz sampling frequency. We observe that for integration times shorter than approximately 2 s, the signal behaviour is dominated by high frequency noise. Increasing the averaging window beyond ~ 2 s reveals the influence of other noise sources, including long-term mechanical drifts in the optical path lengths. We estimate that the sensitivity of our instrument is of 1 mK per piezo cycle (at 40 Hz), and up to 5 μ K for 10 s integration time.

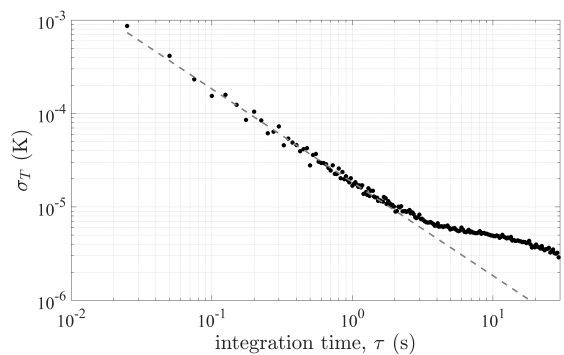


Fig. 3 Allan deviation plot for the static fluid setting, slope τ^{-1} shown as dashed line.

4 Convective flow experiment

In this section we describe the measurements of rapid temperature variations due to natural convection induced by a heating rod in the fluid. Interferometry results are compared against those from RTD sensors. Our interpretation of the measurements obtained is enhanced via numerical simulations and Particle Image Velocimetry.

4.1 Experimental setup

The experimental setup is depicted in Figure 1. The data acquisition device used for this experiment is a Red Pitaya 125-10 (a 10-bit data logger) to facilitate continuous high-frequency data streaming for rapidly fluctuating water temperature measurements. The tank is positioned on a jack lift, with a rectangular opening in the optical table allowing for horizontal and vertical adjustments to sample data from various locations without necessitating laser realignment. The tank geometry is based on that reported by Park et al (2019) and is shown in Fig. 4. The material is common glass with a nominal thickness of 10 mm. The tank is filled with water up to 20 cm and the power output from the heater is set to 12 W. For analysis and comparison against RTD measurements, six different locations were chosen as illustrated in Fig. 4. Some of these points are right above the heater, while others are slightly off. This is done to capture qualitatively different parts of the experiment; e.g. unlike locations 4-6, the area right above the heater (locations 1-3) is expected to be strongly dominated by the rising plume (see Fig. 7).

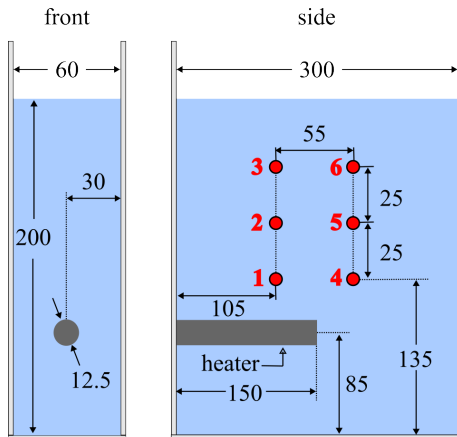


Fig. 4 Sketch of the water tank used in the convective flow experiments showing geometrical details and location of all six points sampled (in red). All dimensions in mm.

As we show later, a short-duration experiment is not appropriate to compare interferometric measurements against those from RTD sensors due to the latter's slow response time. For this reason, experiments were conducted over a 480 s time span. Data collection began right after switching on the heater, which was then switched off at $t = 80$ s, and data recording continued for another 400 s. Therefore, while instantaneous temperature is not expected to be the same for both methods (given their different response times), the final recorded temperature should in theory match (by design, we take the initial temperature to be the same in both methods).

4.2 Results

4.2.1 Comparison against RTD sensors

Comparison between the RTDs and interferometry in six locations within the tank for the convective flow experiment is illustrated in Figure 5. Overall, both methods agree well (especially if the RTDs accuracy is taken into account, which is of ± 0.04 K). However, it is worth analysing several aspects in detail. First of all, all six sampled locations exhibit a high degree of agreement between both techniques at the end of the experiment. This is important because the proposed interferometric method works (i.e. yields instantaneous temperature) by accumulating temperature changes relative to the previous instant in time (piezo stroke), such that if major errors occurred, these would be evident from the final temperature measurement.

We are thus confident that such error accumulation does not take place. Secondly, in all locations a lag between both methods is evident, with temperature peaks being smoothed out and recorded later by the RTDs (this is particularly clear in location 4). This is an expected behaviour given the well-known slow response time of RTDs. We can further verify this by applying a simple moving average function to the original interferometric measurements, which closely replicates the RTD data, as illustrated in Fig. 6 (evidently, this agreement could improve if a different moving average filter, better mimicking the RTDs behaviour, were employed). Finally, notice that rapid temperature variations are not captured by the RTDs, which is especially evident in location 1, where interferometry reports a sharp rise of about 0.23 K within 1.0 s, followed by a decrease in temperature. This phenomenon, also observed in location 2, is presumably caused by the rising plume, and we further analyse it in Section 4.2.2. Temperature fluctuations are also present in locations 3 and 6, which we attribute to the plume's transition to turbulent flow as it approaches the free surface. Locations 4 and 5 do not exhibit the aforementioned discrepancy between techniques due to the the primary mode of heat transfer in these locations, which is conduction rather than convection, leading to the absence of the sharp increases observed in other locations.

4.2.2 Comparison against PIV and LES

The temperature variations measured in locations 1 and 2 at around $t = 30$ s are particularly intriguing, as interferometry not only reveals a rapid increase in temperature due to the rising plume, but also uncovers three peaks within it (see insets in Figs. 5a and 5b). To investigate further the origin of these peaks, we analyse the setup using Particle Image Velocimetry (PIV) and Large Eddy Simulations (LES), focusing our attention on a cross-section normal to the heating rod passing through locations (beam paths) 1, 2 and 3, as illustrated in Fig. 7 (see Appendices A and B for technical details on the PIV and LES settings, respectively).

Fig. 8 shows velocity magnitude and temperature contour plots obtained from PIV and LES in the plane of interest. There are several reasons to expect quantitative discrepancies between

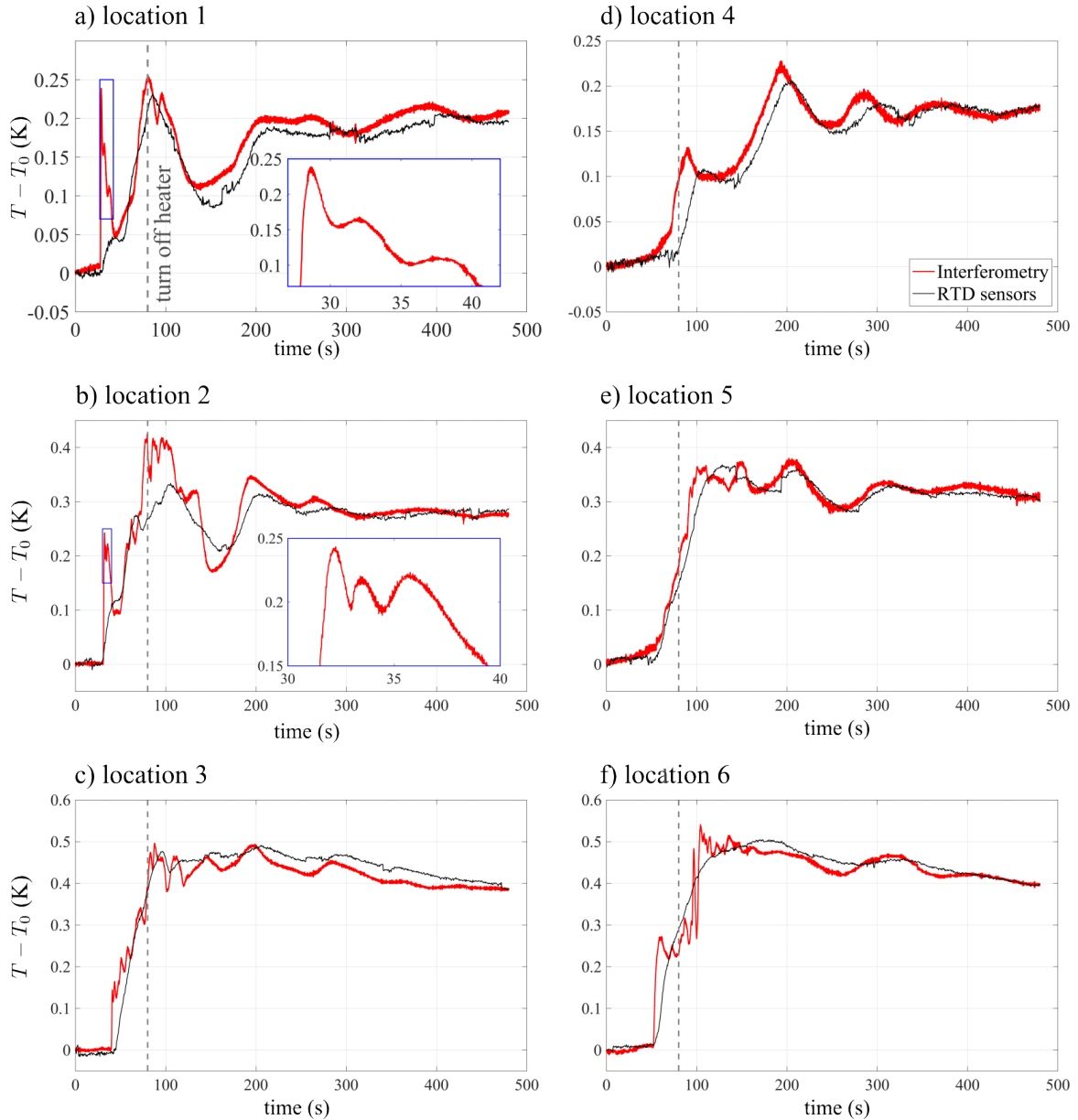


Fig. 5 Temperature change relative to initial temperature, $T - T_0$, for the convective flow experiment. Vertical dashed line represents the time at which the heater was turned off. RTD data (black line) denotes the average of all 4 RTD sensors. Insets in a) and b) are further analysed in Section 4.2.2 and Fig. 8.

PIV and LES. For example, LES assumes a uniform heat flux distribution from the heating rod; however, we observed a marked non-uniformity in temperature employing an infrared camera in the lab (see Fig. 7b). Nevertheless, a qualitative interpretation of these results is sufficient to substantiate our forthcoming arguments.

Comparison of velocity magnitude obtained by LES and PIV shows a good qualitative agreement,

particularly regarding the time of arrival of the plume's front to location 1. In the LES temperature plot, this hot water front is very clear (see Fig. 8a3), such that we can reliably associate it with the first peak detected via interferometry (see Fig. 5a). At this point, it is worth recalling that our method captures the average temperature change along the laser path in the water. Therefore, as the plume progresses upwards, the

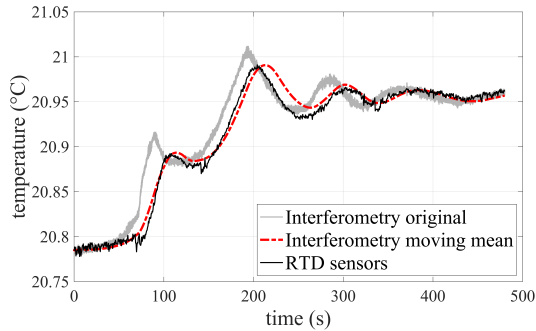


Fig. 6 Measurements from RTDs and interferometry in location 4 after applying a simple moving average function to the interferometry results. Here, the moving-mean temperature reported (red dashed line) at time t represents the average of the previous ~ 30 s.

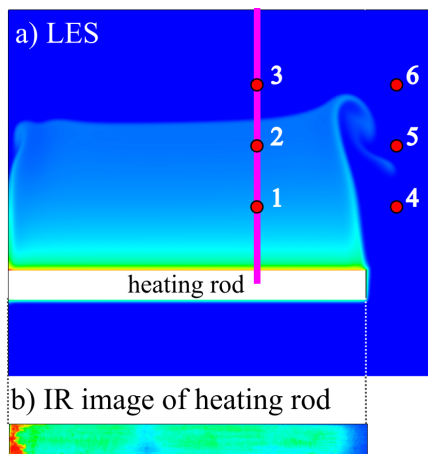


Fig. 7 a) Illustration of a Large Eddy Simulation (temperature field), indicating the location of the cross-section of interest (purple vertical line), which has also been analysed by means of Particle Image Velocimetry (see Fig. 8). b) Non-uniform temperature distribution observed in the heating rod using an infrared (IR) camera. Images provided for qualitative analysis only (hence, no colour bar).

laser at location 1 travels through the thin central ‘neck’ and lateral ‘arms’ of the plume (Fig. 8b3), detecting a decrease of temperature, until the counter-rotating vortices at the edge of the arms reach this location (Fig. 8c3), leading to the detection of a second peak. To explain then the third peak in Fig. 5a (inset), we notice the asymmetry in the rising plume observed via PIV (Figs. 8b1 and 8c1), which is to be expected given the system’s sensitivity to initial conditions (Narayan et al, 2017), as well as imperfections, such as the heat flux non-uniformity discussed above. Because

of this asymmetry, a third peak is detected, corresponding (in this case) to the left-arm eddy, which reaches location 1 with a time delay relative to the right-arm eddy (compare positions of dotted white circles in Figs. 8c1 and 8c2). Additional support for this interpretation comes from the fact that multiple repetitions of this experiment consistently revealed the presence of the aforementioned three peaks at locations 1 and 2 almost every time, but, crucially, not always. Sometimes only two peaks would be detected, which can be attributed to conditions when the plume’s asymmetry was negligible. This method’s sensitivity thus allows us to capture the signature of fine fluid dynamical patterns in a fully non-intrusive manner.

4.3 Thermal shock effect on interference visibility

During the convective flow experiment, the interference visibility γ (see Fig. 1b) decreases substantially when the thermal plume reaches the measurement location, as indicated by the blue circle in Fig. 9a. We claim that this effect is caused by the large vertical temperature gradient across the laser beam induced by the thermal plume’s front, causing significant refraction of the probe beam and subsequent misalignment with the reference beam at the photodetector. This hypothesis is confirmed by recording the beam’s position using a camera, the results of which are shown in Fig. 9b. Note that despite the reduced visibility periods observed in Fig. 9a, we are still able to track the same visibility peak and measure temperature change reliably in the convective flow setting. In other words, the visibility drop does not lead to accumulation of measurement errors, as discussed in Section 4.2.1. However, in other experimental settings (e.g. a stronger plume presenting a temperature gradient closer to an actual thermal shock), visibility reduction can lead to temporary data loss. This makes visibility reduction due to thermal gradients a useful indicator of measurement performance. If the thermal gradient is excessive, our method will provide no data, instead of yielding a distorted measurement. This feature distinguishes the present approach (SI) from holographic interferometry, where refraction (due to the thermal gradients in the fluid) can lead to phase reconstruction errors (Lira and Vest, 1987), and renders

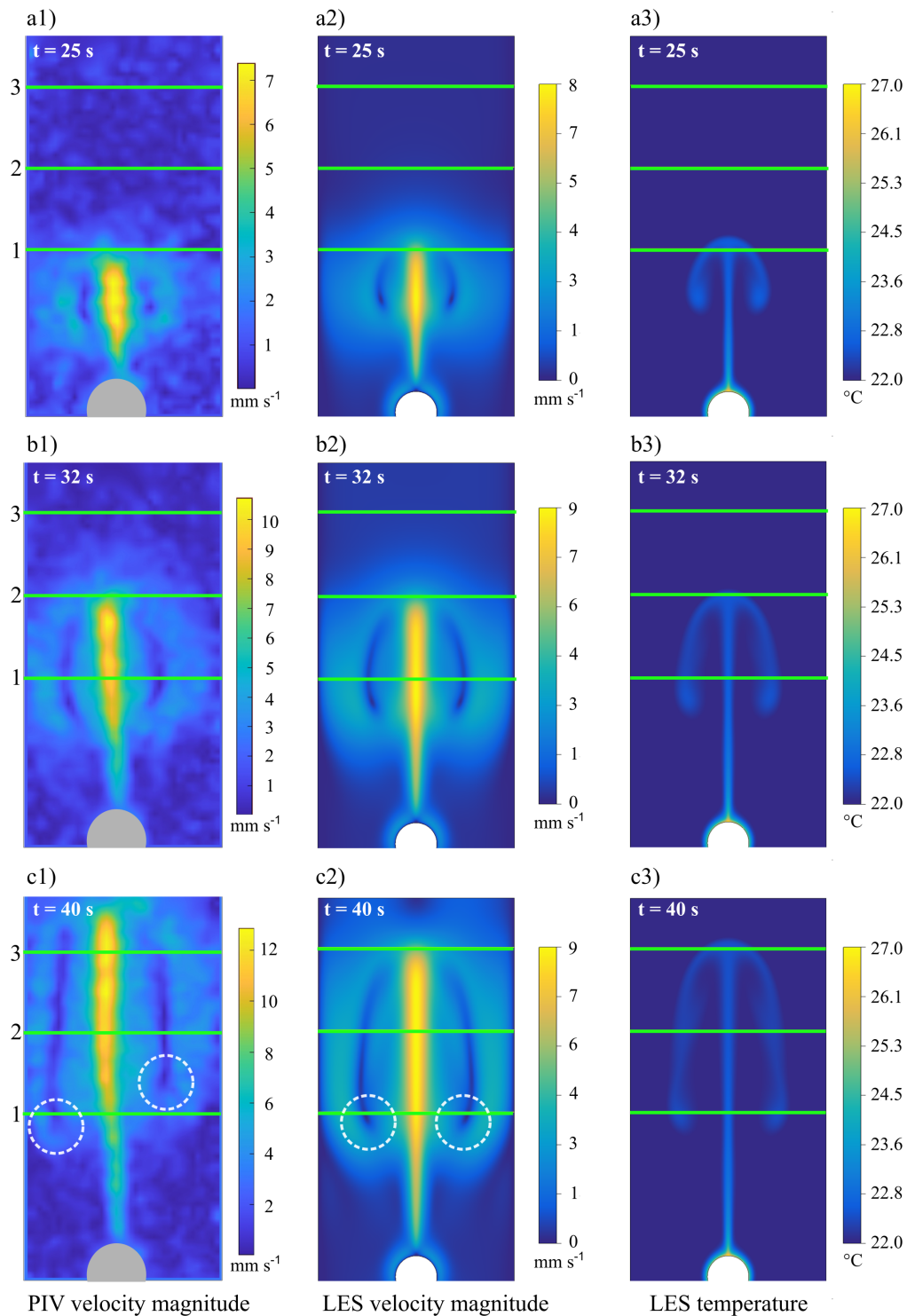


Fig. 8 Velocity magnitude obtained via Particle Image Velocimetry (left panels) and Large Eddy Simulations (centre panels), as well as temperature contour plots from LES (right panels), at three different times after start of the experiment: a) 25 s, b) 32 s, and c) 40 s. The green horizontal lines represent the laser path at locations 1, 2 and 3. Note, the grey semicircle in the PIV images represents the ‘mask’ used for image processing, not the cross-sectional area of the heating rod (which is shown in white in the LES images). From PIV results, an asymmetry in the rising plume is evident.

SI especially suitable for probing rapid temperature changes in three-dimensional flows like the one herein considered.

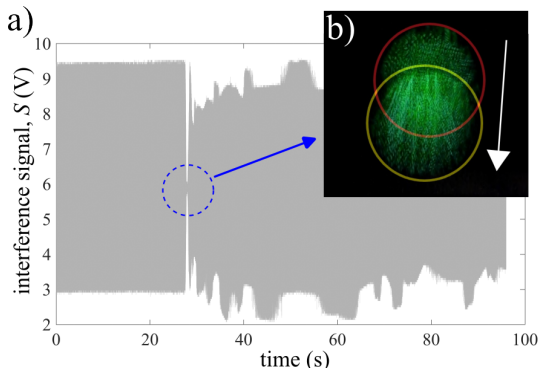


Fig. 9 a) Interference signal detected by the PD at location 1, indicating the drop in visibility γ (blue dashed circle) caused by the arrival of the plume’s front (see inset in Fig. 5a). b) We use a camera to record the temporary change in the probe beam’s position due to refraction, shown by the red (original/permanent position) and yellow (temporary/displaced position) circles; compare with inset in Fig. 1c.

5 Conclusions

We detect rapid temperature changes in water at mK sensitivity in a fully non-intrusive manner. This is achieved by employing standard interferometry, which detects minute temperature-induced changes in the fluid’s refractive index (integrated over the probe beam path). The merits of this technique are demonstrated both for slow-varying temperature in static fluid and for rapid temperature variations in natural convective flow. We achieve a remarkable accuracy of about 1 mK per measurement with a sampling rate of 40 Hz. The high sensitivity and fast response time of our method enable us to capture the signature of fine fluid dynamical patterns that cannot be resolved with traditional methods such as RTD sensors. For example, in convective flow induced by a horizontal heating rod, we observe an asynchronous arrival of two counter-rotating vortices at the measurement location, revealing an asymmetric thermal plume, which we further corroborate by means of Particle Image Velocimetry and Large Eddy Simulations.

Resolving the thermal quasi-shock induced by the rising plume is particularly challenging for any temperature measurement technique. For

example, RTD sensors, in addition to being intrusive, are unable to capture this phenomenon due to their relatively slow response time, whereas Holographic Interferometry based methods cannot reliably operate in the presence of large thermal gradients inherent to the rising plume. Conversely, we are able to capture said near-shock thanks to the fast response and robustness of our approach.

The technique herein described may be utilised to investigate rapid fluid temperature variations on a minuscule scale, such as energy dissipation in eddies, or for validating computational fluid dynamics (CFD) models, offering benefits over conventional methods due to its non-intrusive nature, small data processing requirements and the provision of real-time, highly accurate results.

Appendix A PIV settings

A green laser (532 nm) with an output power of 4.5 mW is used as the source, and a cylindrical lens is employed to generate the light sheet necessary for Particle Image Velocimetry. A high-speed CMOS camera (Baumer VCXU-15M) was utilised to capture particle images at 100 frames per second. A bandpass filter was placed in front of the camera to eliminate ambient light and ensure that only the scattered green light from the tracer particles was captured. Preliminary tests indicated that the maximum velocity magnitude was approximately 10 mm/s. As suggested by Lu and Sick (2013), particle displacements between subsequent frames should not exceed 1/4 of the interrogation window size (8 pixels in our configuration) to reduce the number of pairing loss (loss of particle images within the interrogation window between subsequent frames). The time required for a particle to move 8 pixels is 0.07 s for the maximum expected velocity, which is much larger than the time between adjacent frames for our configuration (0.01 s), indicating that our chosen frame rate is suitable.

Image processing was performed using PIVlab (Thielicke and Stamhuis, 2014). A multi-pass interrogation algorithm with window deformation was implemented to improve the calculation accuracy of the velocity field. Three passes were used in total, which are 128×128 , 64×64 and 32×32 pixels with a 50% overlap. To investigate the influence of the number of passes, we compare the velocity magnitude in a selected point (along location 1

and just above the heating rod) obtained by also using 2 passes only (128×128 and 64×64 pixels) and 4 passes (128×128 , 64×64 , 32×32 and 16×16 pixels). Results are shown in Fig. A1. We observe that 2-passes produces lower velocities compared to the other two settings, while 4-passes introduces the most noise. Thus, in this paper, we report results using the 3-pass interrogation algorithm.

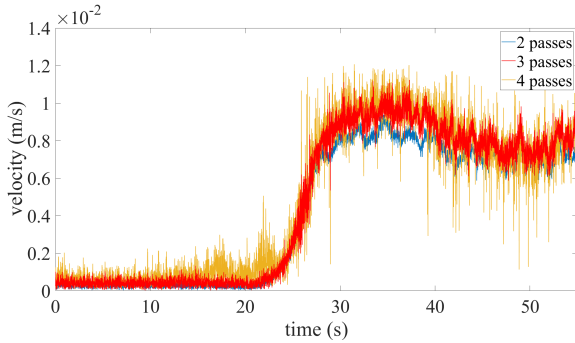


Fig. A1 Velocity magnitude at a point along location 1 and just above the heater, obtained by using three different pass settings when processing PIV images.

Appendix B LES settings

The computational domain in the simulation is set to match our experimental settings, as detailed in Fig. 4. The Navier-Stokes equations are solved using a Large Eddy Simulation (LES) approach with Boussinesq approximation, and the subgrid-scale (SGS) turbulence was modelled using the dynamic Smagorinsky model. The mesh grid has a total number of 40×10^6 hexagonal cells. The minimum grid size is 0.03 mm, and the non-dimensional wall distance y^+ on the heating rod is 0.023. For the boundary conditions, we assign no-slip conditions to the side and bottom walls, while the top wall is designated as a free-slip boundary, considering the fact that any free surface level fluctuations that may occur will be negligible in magnitude compared with the water depth (McSherry et al, 2017). We set the heater's boundary condition as a no-slip wall and define a constant heat flux of 1504 Wm^{-2} , in line with the experiment's power output of 12 W. The initial temperature is set to 22°C everywhere. Simulations are carried out in ANSYS Fluent 21.2. The numerical algorithm and solver settings were adapted from Ma and He (2021), who also analysed a similar

case study using LES. A pressure-based solver was employed, and SIMPLEC scheme was used for the pressure-velocity coupling scheme. Discretisation of the gradients and pressure equation was conducted by least squares cell based and body force weighted scheme, respectively. For the momentum and energy equations, boundary central differencing and second order upwind schemes are adopted, respectively. Time marching is achieved by a bounded second order implicit scheme. The simulations were run on the University of Southampton's Iridis 5 supercomputer.

To determine the integration time step, Fig. B2 illustrates the mean velocity magnitude along location 2 (that is, averaged over the beam path at location 2) for three different values of the time step. The decrease in time step from 0.01 to 0.005 s yields a marginal mean difference of only 0.24%. In contrast, a reduction in the time step from 0.05 to 0.01 s results in a larger mean difference of 1.79%. Therefore, we conclude that the benefits of the additional computational time and resources required for smaller time steps beyond 0.01 s are not justified. Hence, we determine that a time step of 0.01 s provides sufficient precision for our needs and was consequently selected for our simulations.

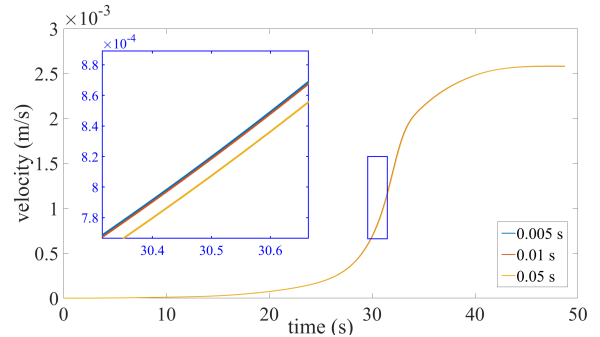


Fig. B2 LES-obtained mean velocity magnitude along location 2 (i.e. averaged over the beam path at location 2) for three different time steps.

The quality of the LES computational grid was judged based on a Reynolds-Averaged Navier-Stokes (RANS) simulation of the same case. The turbulent integral length scale, $l_1 = k^{3/2}/\varepsilon$ (where k and ε are the turbulent kinetic energy and energy dissipation rate, respectively), was derived from the RANS simulation and served as a benchmark for assessing the quality of the mesh. The LES results are deemed satisfactory if more than

80% of the turbulent kinetic energy is resolved. This goal can be achieved by ensuring the filter width, Δ , is smaller than $l_1/12$, as suggested by Pope (2000), where Δ is computed according to the volume of the computational cell, V , using $\Delta = V^{1/3}$. Figure B3 shows the ratio l_1/Δ computed for the grid used in our LES model. The contour range is confined between 0 and 12, such that the grid size in the white area complies with the $l_1/\Delta > 12$ rule, and therefore, the core region of the domain possesses an acceptable resolution. The non-dimensional wall distance, or y^+ , on the heater and the walls is 0.023, which is sufficiently low to ensure a well-resolved LES near the wall.

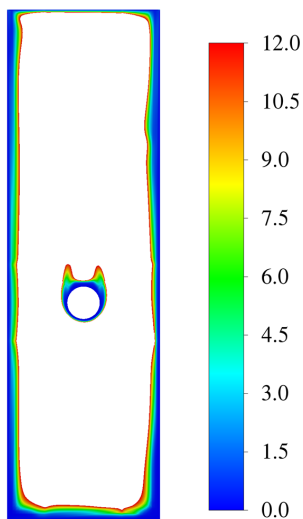


Fig. B3 Contour of the ratio between the RANS integral length scale l_1 and the filter width Δ at 40 s after start of the experiment; the white area complies with the $l_1/\Delta > 12$ rule.

Declarations

Ethical Approval not applicable

Competing interests The authors have no competing interests to declare that are relevant to the content of this article.

Authors' contributions SM and JAZ conceived the research idea. XG performed the experimental work and LES, and processed all data. All authors discussed the results and contributed to the final manuscript.

Funding Partial funding was received from the University of Southampton. XG was partly funded by the University of Southampton through a Presidential Scholarship.

Availability of data and materials Data available from the authors upon request

Acknowledgements The authors acknowledge the use of the IRIDIS High Performance Computing Facility, and associated support services at the University of Southampton, in the completion of this work.

References

- Abram C, Fond B, Beyrau F (2018) Temperature measurement techniques for gas and liquid flows using thermographic phosphor tracer particles. *Progress in energy and combustion science* 64:93–156. <https://doi.org/https://doi.org/10.1016/j.pecs.2017.09.001>
- Allan D (1966) Statistics of atomic frequency standards. *Proceedings of the IEEE* 54(2):221–230. <https://doi.org/10.1109/PROC.1966.4634>
- Ashjaee M, Yousefi T (2007) Experimental study of free convection heat transfer from horizontal isothermal cylinders arranged in vertical and inclined arrays. *Heat transfer engineering* 28(5):460–471. <https://doi.org/https://doi.org/10.1080/01457630601165822>
- Ashjaee M, Eshtiaghi A, Yaghoubi M, et al (2007) Experimental investigation on free convection from a horizontal cylinder beneath an adiabatic ceiling. *Experimental Thermal and Fluid Science* 32(2):614–623. <https://doi.org/https://doi.org/10.1016/j.expthermflusci.2007.07.004>
- Banks D, Robles V, Zhang B, et al (2019) Planar laser induced fluorescence for temperature measurement of optical thermocavitation. *Experimental Thermal and Fluid Science* 103:385–393. <https://doi.org/https://doi.org/10.1016/j.expthermflusci.2019.01.030>

- Childs PR, Greenwood J, Long C (2000) Review of temperature measurement. Review of scientific instruments 71(8):2959–2978. <https://doi.org/https://doi.org/10.1063/1.1305516>
- Ciddor PE (1996) Refractive index of air: new equations for the visible and near infrared. Appl Opt 35(9):1566–1573. <https://doi.org/10.1364/AO.35.001566>, URL <https://opg.optica.org/ao/abstract.cfm?URI=ao-35-9-1566>
- dataTaker (2013) DT80 Range User’s Manual. Thermo Fisher Scientific, Australia
- Drusová S, Bakx W, Doornenbal PJ, et al (2021) Comparison of three types of fiber optic sensors for temperature monitoring in a groundwater flow simulator. Sensors and Actuators A: Physical 331:112,682. <https://doi.org/https://doi.org/10.1016/j.sna.2021.112682>
- Fernández-Prini R, Dooley R (1997) Release on the refractive index of ordinary water substance as a function of wavelength, temperature and pressure. International Association for the Properties of Water and Steam pp 1–7
- Fernandez-Valdivielso C, Matias IR, Arregui FJ, et al (2003) Thermochromic-effect-based temperature optical fiber sensor for underwater applications. Optical Engineering 42(3):656–661. <https://doi.org/https://doi.org/10.1117/1.1541620>
- Goumopoulos C (2018) A high precision, wireless temperature measurement system for pervasive computing applications. Sensors 18(10):5. <https://doi.org/https://doi.org/10.3390/s18103445>
- Guerrero-Mendez C, Anaya TS, Araiza-Esquivel M, et al (2016) Real-time measurement of the average temperature profiles in liquid cooling using digital holographic interferometry. Optical Engineering 55(12):121,730. <https://doi.org/10.1117/1.OE.55.12.121730>
- Herraez J, Belda R (2002) A study of free convection in air around horizontal cylinders of different diameters based on holographic interferometry. temperature field equations and heat transfer coefficients. International journal of thermal sciences 41(3):261–267. [https://doi.org/https://doi.org/10.1016/S1290-0729\(01\)01314-X](https://doi.org/https://doi.org/10.1016/S1290-0729(01)01314-X)
- Kim H, Byun H, Song Y, et al (2018) Multi-channel fiber-optic temperature sensor system using an optical time-domain reflectometer. Results in Physics 11:743–748. <https://doi.org/https://doi.org/10.1016/j.rinp.2018.10.024>
- Laffont G, Cotillard R, Roussel N, et al (2018) Temperature resistant fiber bragg gratings for on-line and structural health monitoring of the next-generation of nuclear reactors. Sensors 18(6):1791. <https://doi.org/https://doi.org/10.3390/s18061791>
- Lira IH, Vest CM (1987) Refraction correction in holographic interferometry and tomography of transparent objects. Appl Opt 26(18):3919–3928. <https://doi.org/10.1364/AO.26.003919>, URL <https://opg.optica.org/ao/abstract.cfm?URI=ao-26-18-3919>
- Lu L, Sick V (2013) High-speed particle image velocimetry near surfaces. JoVE (Journal of Visualized Experiments) 76(50559). <https://doi.org/10.3791/50559>
- Ma H, He L (2021) Large eddy simulation of natural convection heat transfer and fluid flow around a horizontal cylinder. International Journal of Thermal Sciences 162:106,789. <https://doi.org/https://doi.org/10.1016/j.ijthermalsci.2020.106789>
- Mandel L, Wolf E (1995) Optical Coherence and Quantum Optics. Cambridge University Press, United States of America, <https://doi.org/10.1017/CBO9781139644105>
- McSherry RJ, Chua KV, Stoesser T (2017) Large eddy simulation of free-surface flows. Journal of Hydrodynamics, Ser B 29(1):1–12. [https://doi.org/https://doi.org/10.1016/S1001-6058\(16\)60712-6](https://doi.org/https://doi.org/10.1016/S1001-6058(16)60712-6)
- Moldover MR, Gavioso RM, Mehl JB, et al (2014) Acoustic gas thermometry. Metrologia 51(1):R1. <https://doi.org/10.1088/0026-1394/51/1/R1>

- Narayan S, Singh AK, Srivastava A (2017) Interferometric study of natural convection heat transfer phenomena around array of heated cylinders. *International Journal of Heat and Mass Transfer* 109:278–292. <https://doi.org/https://doi.org/10.1016/j.ijheatmasstransfer.2017.01.106>
- Park H, Park J, Jung SY (2019) Measurements of velocity and temperature fields in natural convective flow. *International Journal of Heat and Mass Transfer* 139:292–302. <https://doi.org/https://doi.org/10.1016/j.ijheatmasstransfer.2019.05.022>
- Pope SB (2000) *Turbulent flows*. Cambridge university press, New York
- Rizzolo S, Périssé J, Boukenter A, et al (2017) Real time monitoring of water level and temperature in storage fuel pools through optical fibre sensors. *Scientific Reports* 7(8766):1–10. <https://doi.org/https://doi.org/10.1038/s41598-017-08853-7>
- Roriz P, Silva S, Frazao O, et al (2020) Optical fiber temperature sensors and their biomedical applications. *Sensors* 20(7):2113. <https://doi.org/10.3390/s20072113>
- Ross D, Gaitan M, Locascio LE (2001) Temperature measurement in microfluidic systems using a temperature-dependent fluorescent dye. *Analytical chemistry* 73(17):4117–4123. <https://doi.org/https://doi.org/10.1021/ac010370l>
- Sakakibara J, Adrian R (2004) Measurement of temperature field of a rayleigh-bénard convection using two-color laser-induced fluorescence. *Experiments in fluids* 37(3):331–340. <https://doi.org/10.1007/s00348-004-0821-3>
- Tango WJ, Link JK, Zare RN (1968) Spectroscopy of k₂ using laser-induced fluorescence. *The Journal of Chemical Physics* 49(10):4264–4268. <https://doi.org/https://doi.org/10.1063/1.1669869>
- Taylor AT, Lai EP (2021) Current state of laser-induced fluorescence spectroscopy for designing biochemical sensors. *Chemosensors* 9(10):275. <https://doi.org/https://doi.org/10.3390/chemosensors9100275>
- Thielicke W, Stamhuis E (2014) Pivlab—towards user-friendly, affordable and accurate digital particle image velocimetry in matlab. *Journal of open research software* 2(1). <https://doi.org/10.5334/jors.bl>
- Wang C, Xie X, Zhang H, et al (2022) Single-element real-time interferometric system for measuring dynamic temperature field of liquid medium. *AIP Advances* 12(4):045,010. <https://doi.org/https://doi.org/10.1063/5.0087196>
- Wang Y, Zou F, Cegla FB (2018) Acoustic waveguides: An attractive alternative for accurate and robust contact thermometry. *Sensors and Actuators A: Physical* 270:84–88. <https://doi.org/https://doi.org/10.1016/j.sna.2017.12.049>
- Wilkie D, Fisher SA (1963) Measurement of temperature by mach-zehnder interferometry. *Proceedings of the Institution of Mechanical Engineers* 178(1):461–470. <https://doi.org/10.1177/002034836317800166>
- Wu B, Zhao J, Wang J, et al (2013) Visual investigation on the heat dissipation process of a heat sink by using digital holographic interferometry. *Journal of Applied Physics* 114(19):193,103. <https://doi.org/https://doi.org/10.1063/1.4832479>